Eur. J. Mineral.
2002, **14**, 417–427

This paper was presented at the EMPG VIII
meeting in Bergamo, Italy (April 2000)

Modelling the non-Arrhenian rheology of silicate melts: Numerical considerations

JAMES K. RUSSELL[1], DANIELE GIORDANO[2], DONALD B. DINGWELL[2] and KAI-UWE HESS

[1] Igneous Petrology Laboratory, Earth & Ocean Sciences, The University of British Columbia, Vancouver, B.C., Canada, V6T 1Z4, e-mail: russell@perseus.geology.ubc.ca
[2] Institut für Mineralogie, Petrologie und Geochemie, Ludwig-Maximilians-Universität München, D-80333 München, Germany, e-mail: giordano@, dingwell@petro1.uni-muenchen.de

Abstract: Future models for predicting the viscosity of geologically relevant silicate melts must find a means of partitioning the effects of composition across a system that shows varying degrees of non-Arrhenian temperature dependence. In the short term, the decisions governing how to expand the non-Arrhenian parameters in terms of composition will probably derive from empirical study. The non-linear character of the non-Arrhenian models ensures strong numerical correlations between model parameters which may mask the effects of composition. We present a numerical analysis of the nature and magnitudes of correlations inherent in fitting a non-Arrhenian model (*e.g.*, Tamman-Vogel-Fulcher function) to published measurements of melt viscosity. Furthermore, we demonstrate the extent to which the quality and distribution of experimental data can affect covariances between model parameters. The extent of non-Arrhenian behaviour of the melt also affects parameter estimation. We explore this effect using albite and diopside melts as representative of strong, nearly Arrhenian melts and fragile, non-Arrhenian melts, respectively. The magnitudes and nature of these numerical correlations tend to obscure the effects of composition and, therefore, are essential to understand prior to assigning compositional dependencies to fit parameters in non-Arrhenian models.

Key-words: viscosity, silicate-melts, non-Arrhenian, data-analysis, model-estimation.

Introduction

Viscosity is probably the single most important physical property governing the formation, transport and eruption of naturally occurring silicate melts or magmas. It is, therefore, surprising that Earth science does not have an accurate means of forecasting the viscosity of silicate melts over the full range of compositions and temperatures found in nature. More than twenty-five years ago Shaw (1972) and Bottinga & Weill (1972) published empirical methods for computing silicate melt viscosities as a function of temperature (T) and composition. Their models were built on an experimental database that was limited in three main ways. Firstly, the database was small, constituting less than 2600 measurements. Secondly, their experimental data did not completely overlap or span the range of natural melt compositions. Thirdly, the majority of data derived from liquidus or super-liquidus experiments. On this basis, both Shaw (1972) and Bottinga & Weill (1972) adopted an Arrhenian temperature dependence for melt viscosities (η):

$$\log \eta \text{ [Pa s]} = \mathbf{A} + \frac{\mathbf{B}}{T} \qquad (1)$$

where **A** and **B** are parameters that vary as a function of melt composition and T is temperature in kelvins. The seminal contribution made by these two papers was to provide a basis for predicting the values of **A** and **B** as a function of melt composition.

The total number of published viscosity measurements on silicate melts has increased greatly in recent years. Experiments cover a wider range of composition and temperature, but more importantly, the experiments sample a greater range of melt viscosities (see Dingwell, 1998; Richet & Bottinga, 1995). These data serve two purposes. Firstly, they demonstrate the inadequacies of the earlier models, in particular, the fact that models for natural systems must accommodate non-Arrhenian temperature dependence. Secondly, the volume and quality of the experimental data provide a basis for forming more robust models for predicting viscosity as a function of temperature, composition and pressure (*e.g.*, Richet, 1984; Persikov, 1991; Richet & Bottinga, 1995; Baker, 1996; Hess & Dingwell, 1996; Toplis *et al.,* 1997; Toplis, 1998; Giordano *et al.,* 2000).

The main challenge to modelling viscosity in natural systems is devising a rational means for distributing the effects of melt composition across the non-Arrhenian model pa-

DOI: 10.1127/0935-1221/2002/0014-0417

0935-1221/02/0014-0417 $ 4.95

rameters (*e.g.*, Richet, 1984; Richet & Bottinga, 1995; Hess *et al.,* 1996; Toplis *et al.,* 1997; Toplis, 1998; Rossler *et al.,* 1998; Persikov, 1991; Prusevich, 1988). For example, the purely empirical Tamman-Vogel-Fulcher (TVF) expression:

$$\log \eta = \mathbf{A} + \frac{\mathbf{B}}{\mathrm{T}-\mathbf{C}} \qquad (2)$$

introduces three fit parameters (**A**, **B**, **C**); the values of these parameters vary with melt composition. At present, there is no theoretical means of establishing *a priori* the forms of compositional dependence for these model parameters.

In this paper we explore the numerical consequences of fitting viscosity-temperature datasets to non-Arrhenian rheological models. Our analysis shows that strong correlations and even non-unique estimates of model parameters (*e.g.*, **A**, **B**, **C**) are inherent to non-Arrhenian models. Furthermore, uncertainties on model parameters and covariances between parameters are strongly affected by the quality and distribution of the experimental data, as well as the degree of non-Arrhenian behaviour. These correlations serve to mask the independent relationships between melt composition and the values of **A**, **B**, and **C**. This work constitutes a starting point in the ultimate goal of predicting viscosity as a function of melt composition and temperature in natural systems. We strongly suggest that it is critical to evaluate the nature of these model- or data-induced covariances before we develop models for how **A**, **B**, and **C** (or other non-Arrhenian parameters) vary with composition.

Computational strategy

Future models for predicting the viscosity of natural melts face the challenge of accommodating 10-12 components in order to span the full compositional range found in nature. The task is further complicated because naturally occurring silicate melts show varying degrees of non-Arrhenian behaviour. Strong liquids that are highly polymerized (*e.g.*, rhyolite melts), as well as high-temperature melts, can show near-Arrhenian temperature dependence. Conversely, more "fragile" liquids (*e.g.*, basalt, basanite, hydrous melts) can behave strongly non-Arrhenian over geological ranges of temperature. Predictive models must span the full spectrum of rheological behaviour shown by natural melts, and must be able to model in a continuous manner extreme changes in behaviour resulting from changes in melt composition (*e.g.*, fractionation or vesiculation).

There is substantial recent literature concerning viscosity-T relationships of non-Arrhenian silicate melts (*e.g.*, Richet, 1984; Hess *et al.,* 1996; Rossler *et al.,* 98; Toplis *et al.,* 1997). Richet & Bottinga (1995), for example, provide an excellent review of the rationales behind the basic equations. For the purposes of this analysis, we have adopted the Tamann-Vogel-Fulcher equation (TVF: Fulcher, 1925), but our results are equally relevant to other non-Arrhenian functions (*e.g.*, Adam-Gibbs (AG), Adam & Gibbs, 1965; mode-coupling theory (MCT), Angell, 1988). Regardless of which of the three main functions are employed (TVF, AG or MCT), the non-Arrhenian model increases the complexity of how we address the compositional controls on viscosity.

In the short term, at least, strategies for partitioning the effects of composition across any non-Arrhenian model are likely to be empirical. Estimates of the parameters **A**, **B** and **C** in the TVF model, for example, can be derived for a single melt composition by fitting Eq. 2 to datasets of T(K)-log [η] (Fig. 1). Parameter values from a variety of melt compositions can then be mapped against compositional properties to produce functional relationships between the model parameters (*e.g.*, **A**, **B** and **C**; Eq. 2) and composition (*e.g.*, Cranmer & Uhlmann, 1981; Richet & Bottinga, 1995; Hess *et al.,* 1996; Toplis *et al.,* 1997; Toplis, 1998).

It is unlikely that all three model parameters will prove to be linearly dependent on composition. For example, detailed studies of several simple chemical systems show the parameter values to have a non-linear dependence on composition (Cranmer & Uhlmann, 1981; Richet, 1984; Hess *et al.,* 1996; Toplis *et al.,* 1997; Toplis, 1998). Additionally, there are empirical data and a theoretical basis indicating that the parameters **A**, **B** and **C** are not equally dependent on composition (Richet & Bottinga, 1995; Hess *et al.,* 1996; Rossler *et al.,* 1998; Toplis *et al.,* 1997; Giordano *et al.*, 2000). Values of **A** in the TVF model, for example, represent the high-temperature limiting behaviour of viscosity and tend to have a narrow range of values over a wide range of melt compositions (*e.g.*, Shaw, 1972; Cranmer & Uhlmann, 1981; Hess *et al.,* 1996; Richet & Bottinga, 1995; Toplis *et al.,* 1997; Giordano *et al.*, 2000). The parameter **C** has units of temperature in kelvins and is constrained to be positive in value. As values of **C** approach zero, the melt tends to become increasingly Arrhenian in behaviour. Values of **B** are also required to be greater than zero if viscosity is to decrease with increasing temperature. It may be that the parameter **A** is less dependent on composition than **B** or **C**; it may even be a constant for silicate melts.

Below we use three experimental datasets to explore the nature of covariances that arise from fitting the TVF equation (Eq. 2) to viscosity data collected over a range of temperatures. The three parameters (**A**, **B**, **C**) to the TVF equation are solved for by minimization of the χ^2 function:

$$\chi^2 = \sum_{i=1}^{n} \left[\frac{\log \eta_i - \mathbf{A} - \frac{\mathbf{B}}{\mathrm{T}_i - \mathbf{C}}}{\sigma_i} \right]^2 . \qquad (3)$$

The objective function is weighted to uncertainties (σ_i) on viscosity arising from experimental measurement. The form of the TVF function is non-linear with respect to the unknown parameters and, therefore, Eq. 3 is solved by conventional iterative methods (*e.g.*, Press *et al.,* 1986).

The solution surface to the χ^2 function (Eq. 3) is 3-dimensional (*e.g.*, 3 parameters) and there are other minima to the function that lie outside the range of realistic values of **A**, **B** and **C** (*e.g.*, **B** and **C** > 0). We have taken the usual cautionary steps to ensure that the global minimum was obtained within the appropriate solution space. In general, convergence to a stable minimum was achieved in less than 20 iterations. Upon achieving the minimum, the solution was perturbed (2-5 %) in each parameter to test that the same solution was recovered. We also checked that the first derivative

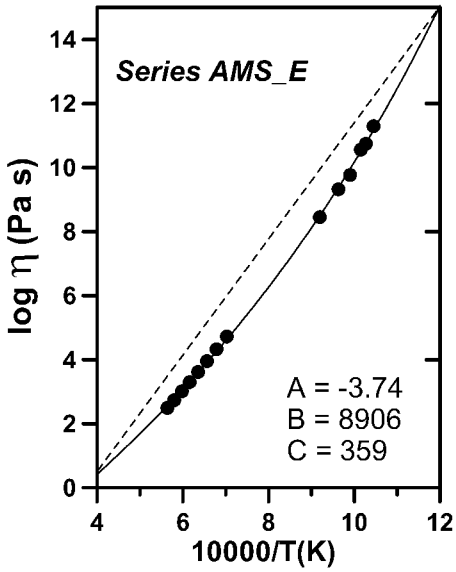

Fig. 1. Experimental measurements of viscosity for alkali trachyte melts (Table 1; AMS_E) are shown as log [η(Pa s)] *vs.* 10,000/T (K) and fitted to the TVF function (solid line; Table 2). An equivalent melt showing idealized Arrhenian behaviour is represented by the dashed line.

Table 1. Measured values of viscosity (N=14) as a function of temperature for alkali-trachyte melts (AMS_E; C. Romano pers. comm. 2000) containing < 0.2 wt. % dissolved H_2O. Viscosity was measured on samples of hydrous glass by micropenetration methods described in Hess *et al.* (1995) and Dingwell (1993). High temperature viscosity data (10^0-10^5 Pa s) were measured using concentric cylinder apparatus.

Oxide	Wt. %	T (K)	log η (Pa s)[1]	10,000/(T (K))
SiO_2	59.98	973.2	10.75	10.27
TiO_2	0.39	956.8	11.29	10.45
Al_2O_3	18.01	1087.1	8.45	9.20
FeO	3.82	985.0	10.56	10.15
MnO	0.11	1009.6	9.77	9.91
MgO	0.88	1038.3	9.32	9.63
CaO	2.91	1773	2.49	5.64
Na_2O	4.06	1723	2.74	5.80
K_2O	8.37	1673	3.01	5.98
P_2O_5	0.21	1623	3.30	6.16
H_2O[1]	0.02	1573	3.62	6.36
		1523	3.96	6.57
		1473	4.33	6.79
		1423	4.73	7.03

[1] Mean experimental uncertainty (1σ) of viscosity measurements is 0.15 in units of log η (Pa s).

of the χ^2 function with respect to each parameter was numerically zero at the solution. Lastly, we computed and contoured the χ^2 surface over a range of values **A**, **B** and **C** to ensure coincidence between the numerical and graphical minima (*e.g.*, Fig. 2).

One attribute of using the χ^2 merit function is that, rather than consider a single solution that coincides with the minimum residuals, we can map a solution region at a specific confidence level (*e.g.*, 1σ; Press *et al.*, 1986). This allows delineation of the full range of parameter values (*e.g.*, **A**, **B**, and **C**) that can be considered equally valid descriptors of the experimental data at the specified confidence level (*e.g.*, Russell & Hauksdóttir, 2001; Russell *et al.*, 2001).

Model-induced covariances

The first data set comprises 14 measurements of viscosity (Fig. 1) for an alkali-trachyte composition over a temperature range of 973-1773 K (Table 1; Romano pers. comm. 2001). The experimental data span a wide enough range of temperature to show non-Arrhenian behaviour (Table 1, Fig. 1). The gap in the data between 1100 and 1420 K is a region of temperature where the rates of vesiculation or crystallization in the sample exceed the timescales of viscous deformation. The corresponding TVF parameters computed from these data are: **A** = -3.74, **B** = 8906, and **C** = 359 (Table 2; Fig. 1, solid line).

Analysis of covariance

Fig. 2 is a series of 2-dimensional (2-D) maps showing the characteristic shape of the χ^2 function (Eq. 3). The three maps are mutually perpendicular planes that intersect at the optimal solution and lie within the full 3-dimensional solution space. These particular maps explore the χ^2 function over a range of parameter values equal to ± 75 % of the optimal solution values. Specifically, we have calculated the values of the χ^2 function away from the optimal solution by holding one parameter constant (*e.g.*, **C** = 359 in Fig. 2a) and by substituting new values for the other two parameters. The contoured versions of these maps simply show the 2-dimensional geometry of the solution surface.

These maps illustrate several interesting features. Firstly, the shapes of the 2-D solution surfaces vary depending upon which parameter is fixed. At a fixed value of **C**, coinciding with the optimal solution (Fig. 2a), the solution surface forms a steep-walled, flat-floored and symmetric trough with a well-defined minimum. Conversely, where **A** is fixed (Fig. 2b), the contoured surface shows a symmetric but fanning pattern; the χ^2 surface dips slightly to lower values of **B** and higher values of **C**. Lastly, where **B** is held constant (Fig. 2c), the solution surface is clearly asymmetric but contains a well-defined minimum. Qualitatively, these maps also indicate the strength of correlations between pairs of model parameters at the solution (see below).

The nature of correlations between model parameters arising from the form of the TVF equation is explored more quantitatively in Fig. 3. Specifically, we have calculated and mapped the linear approximations to the 1σ confidence limits on the solution (Press *et al.,* 1986; see Appendix 1). The same data as contoured in Fig. 2 are represented by the solid, smaller ellipses in each of the 2-D projections (Fig. 3a, b, c). These smaller ellipses correspond exactly to a specific contour level ($\Delta\chi^2$ = 16.4; Table 2) and approximate the 1σ confidence limits for two parameters, if the 3rd parameter is fixed at the optimal solution (see Appendix 1). For example,

Table 2. Results of fitting viscosity data on alkali trachyte (ASM_E; Table 1) to TVF equation.

	Parameter values	3-D_{proj}	2-D error envelopes (1σ) at solution			Covariance		
		1σ[1]	**A**	**B**	**C**	[**A**:i]	[**B**:i]	[**C**:i]
A	-3.74	2.96	-	0.27	0.45	0.70	-1290	60.5
B	8906	5509	498	-	381	-1290	2407926	-113476
C	359	260	39.8	18.0	-	60.5	-113476	5373
min χ^2	3.81[2]							

[1] Approximate 1 standard error estimates of uncertainty on model parameters (see text).
[2] Calculated $\Delta\chi^2$ values for 1σ, 2σ and 3σ confidence limits are 16.4, 23.5 and 28.5, respectively.

the small ellipse in Fig. 3a represents the intersection of the plane **C** = 359 with a 3-D ellipsoid representing the 1 σ confidence limits to the entire solution. It establishes the range of values of **A** and **B** permitted if this value of **C** is maintained**.** Practically, it shows that the experimental data greatly restrict the values of **A** (≈ ± 0.45) and **B** (≈ ± 380), if **C** is fixed (Table 2).

The larger ellipses shown in Fig. 3a, 3b and 3c are of greater significance. They are, in essence, the shadow cast by the entire 3-D confidence envelope onto the 2-D planes containing pairs of the three model parameters. They approximate the full confidence envelopes on the optimum solution. Axis-parallel tangents to these "shadow" ellipses (dashed lines) establish the maximum range of parameter values (*e.g.*, **A**, **B**, **C**) that are consistent with the experimental data at the specified confidence limits. For example, in Fig. 3a, the larger ellipse shows the entire range of model values of **A** and **B** that are consistent with this dataset at the 1 σ confidence level (Table 2).

The covariances between model parameters indicated by the small *vs*. large ellipses are strikingly different. For example, in Fig. 3c the small ellipse shows a negative correlation between **A** and **C** compared to the strong positive correlation indicated by the larger ellipse. This is because the smaller ellipses show the correlations that result when one parameter (*e.g.*, **B**) is held constant at the value of the optimal solution. Where one parameter is fixed, the range of acceptable values and correlations between the other model parameters are greatly restricted. Conversely, the larger ellipse shows the overall correlation between two parameters, whilst the third parameter is also allowed to vary. It is critical to realize that each pair of **A**-**C** coordinates on the larger ellipse demands a unique and different value of **B** (*e.g.*, Fig. 3a, c). Consequently, although the range of acceptable values of **A**:**B**:**C** is large, the parameter values cannot be combined arbitrarily.

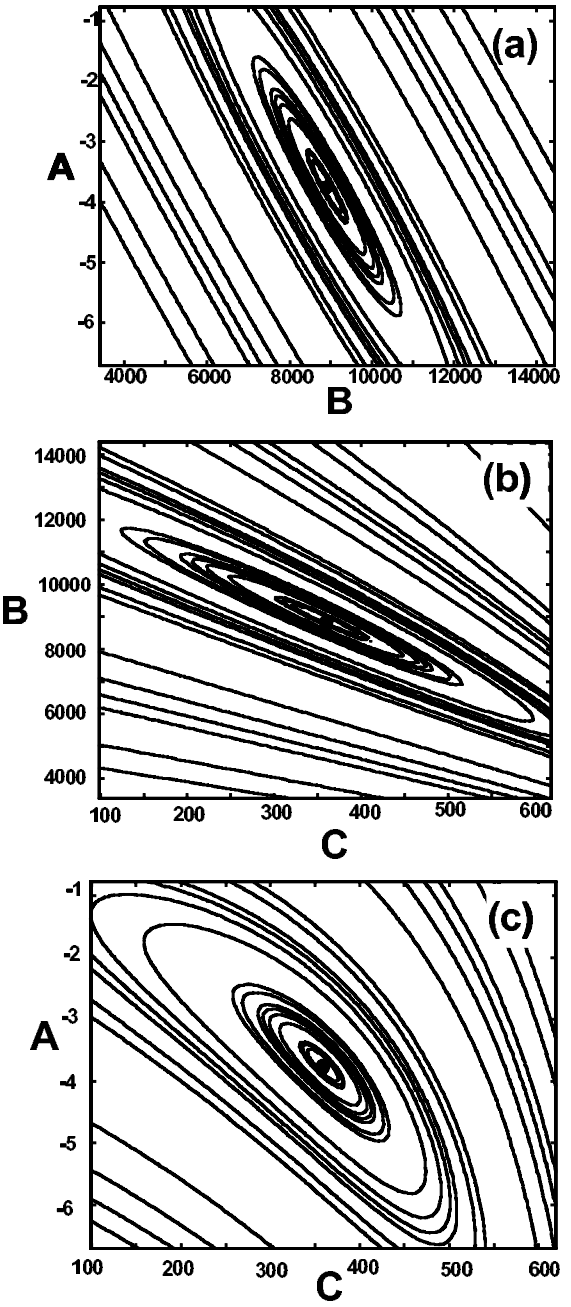

Fig. 2. A contour map showing the shape of the χ^2 minimization surface (Press *et al.,* 1986) associated with fitting the TVF function to the viscosity data for alkali trachyte melt (Fig. 1 and Table 1). The contour maps are created by projecting the χ^2 solution surface onto 2-D surfaces that contain the actual solution (solid symbol). The maps show the distributions of residuals around the solution caused by variations in pairs of model parameters: a) **A**-**B**, b) **B**-**C**, and c) **A**-**C**. Values of the contours shown were chosen to highlight the overall shape of the solution surface.

Model TVF functions

The range of values of **A**, **B**, and **C** shown to be consistent with the experimental dataset (Fig. 1) may seem larger than reasonable at first glance (Fig. 3). The consequences of these results are shown in Fig. 4 as a family of model TVF curves (Eq. 2) calculated by using combinations of **A**, **B**, and **C** that lie on the 1 σ confidence ellipsoid (Fig. 3, larger ellipses). The dashed lines show the limits of the distribution of TVF curves (Fig. 4) generated by using combinations of model parameters **A**, **B** and **C** from the 1 σ confidence limits (Fig. 3). Compared to the original data array and to the

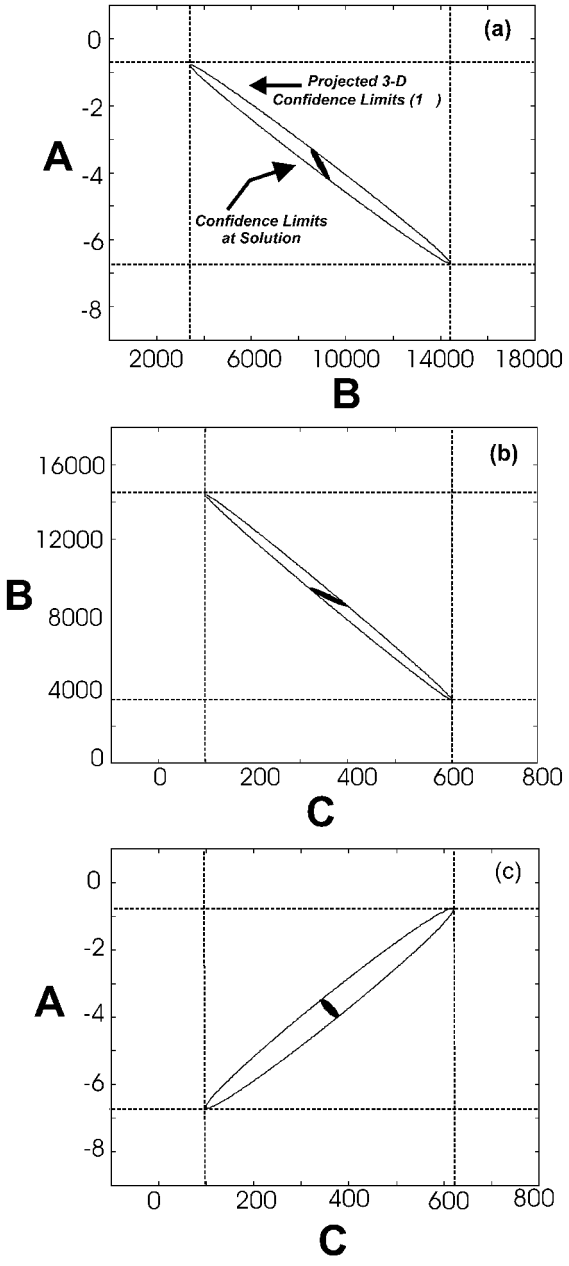

Fig. 3. The solution shown in Fig. 2 is illustrated as 2-D ellipses that approximate the 1 σ confidence envelopes on the optimal solution. The large ellipses approximate the 1 σ limits of the entire solution space projected onto 2-D planes and indicate the full range (dashed lines) of parameter values (*e.g.*, **A**, **B**, **C**) that are consistent with the experimental data. Smaller ellipses denote the 1 σ confidence limits for two parameters where the third parameter is kept constant (see text and Appendix).

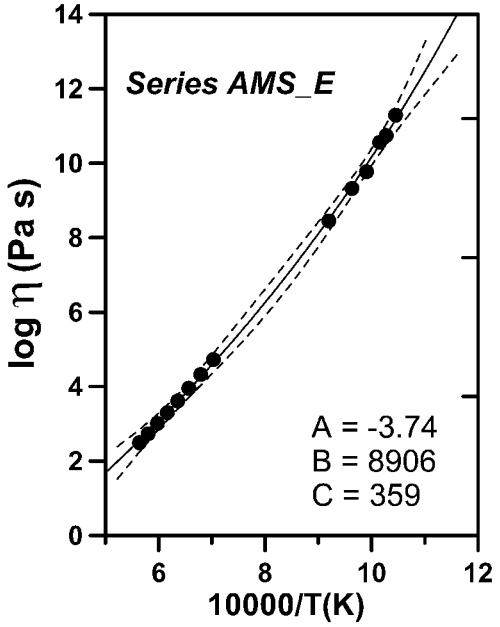

Fig. 4. The optimal TVF function (solid line) and the distribution of TVF functions (dashed lines) permitted by the 1σ confidence limits on **A**, **B** and **C** (Fig. 3) are compared to the original experimental data of Fig. 1.

"best-fit" TVF equation (Fig. 4, solid line), the family of TVF functions describe the original viscosity data well. Each one of these TVF functions must be considered an equally valid fit to the experimental data. In other words, the experimental data are permissive of a wide range of values of **A** (-0.8 to -6.8), **B** (3500 to 14,400) and **C** (100 to 625). However, the strong correlations between parameters (Table 2, Fig. 3) control how these values are combined. The consequence is that, even though a wide range of parameter values are considered, they generate a narrow band of TVF functions that are entirely consistent with the experimental data.

Data-induced covariances

The values, uncertainties and covariances of the TVF model parameters are also affected by the quality and distribution of the experimental data. We demonstrate this concept using published data comprising 20 measurements of viscosity on a Na_2O-enriched haplogranitic melt (Table 3; after Hess *et al.,* 1995; Dorfman *et al.,* 1996). The main attributes of this dataset are that the measurements span a wide range of viscosity (≈ $10\text{-}10^{11}$ Pa s) and the data are evenly spaced across this range (Fig. 5). The data were produced by three different experimental methods, including: concentric cylinder, micropenetration, and centrifuge-assisted falling-sphere viscometry (Table 3, Fig. 5). The latter experiments represent a relatively new experimental technique (Dorfman *et al.,* 1996) that has made the measurement of melt viscosity at intermediate temperatures experimentally accessible.

Our intent is to show the effects of data distribution on parameter estimation. Thus, we have subdivided the data (Table 3) into three subsets; each dataset contains data produced by two of the three experimental methods. A fourth dataset comprises all of the data. The TVF equation has been fit to each dataset and the results are listed in Table 4. Overall, there is little variation in the estimated values of model parameters **A** (-2.35 to -2.85), **B** (4060 to 4784) and **C** (429 to 484).

Table 3. Compilation of viscosity data for haplogranitic melt with addition of 20 wt. % Na_2O. Experimental data include results of high-T concentric cylinder (CC) and low-T micropenetration (MP) techniques and centrifuge assisted falling sphere (CFS) viscometry.

T (K)	log (Pa s)[1]	Method	Source[2]
1571	1.40	CC	H
1522	1.58	CC	H
1473	1.77	CC	H
1424	1.98	CC	H
1375	2.21	CC	H
1325	2.46	CC	H
1276	2.74	CC	H
1227	3.07	CC	H
1178	3.42	CC	H
993	5.73	CFS	D
993	5.58	CFS	D
993	5.60	CFS	D
973	5.99	CFS	D
903	7.29	CFS	D
1043	4.99	CFS	D
1123	4.00	CFS	D
822.5	9.35	MP	H
795.5	10.10	MP	H
777.4	10.90	MP	H
755.4	11.90	MP	H

[1] Experimental uncertainty (1σ) is 0.1 units of log η.
[2] Sources include: (H) Hess *et al.* (1995) and (D) Dorfman *et al.* (1996).

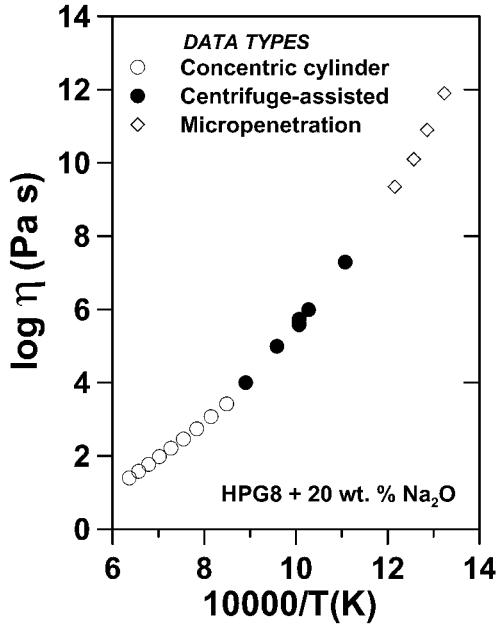

Fig. 5. Viscosity data for a single composition of Na-rich haplogranitic melt (Table 3) are plotted against reciprocal temperature. Data derive from a variety of experimental methods including: concentric cylinder, micropenetration, and centrifuge-assisted falling-sphere viscometry (Hess *et al.,* 1995; Dorfman *et al.,* 1996).

Variance in model parameters

The 2-D projections of the 1 σ confidence envelopes computed for each dataset are shown in Fig. 6. Although the parameter values change only slightly between datasets, the nature of the covariances between model parameters varies substantially. Firstly, the sizes of the ellipses vary between datasets. Axis-parallel tangents to these "shadow" ellipses approximate the ranges of **A**, **B** and **C** that are supported by the data at the specified confidence limits (Table 4 and Fig. 7). As would be expected, the dataset containing all the available experimental data (No. 4) generates the smallest projected ellipse and, thus, the smallest range of **A**, **B** and **C** values. Clearly, more data spread evenly over the widest range of temperatures has the greatest opportunity to restrict parameter values.

The projected confidence limits for the other datasets show the impact of working with a dataset that lacks high-, or low-, or intermediate-temperature measurements. In particular, if either the low-T or high-T data are removed, the confidence limits on all three parameters expand greatly (*e.g.*, Fig. 6 and Fig. 7). The loss of high-T data (No. 1; Fig. 6, 7 and Table 4) increases the uncertainties on model values of **A**. Less anticipated is the corresponding increase in the uncertainty on **B**. The loss of low-T data (No. 2; Fig. 6, 7 and Table 4) causes increased uncertainty on **A** and **B** but less than for case No. 1. However, the 1σ confidence limits on the **C** parameter increase nearly 3-fold (350-600). The loss of the intermediate temperature data (*e.g.*, CFS data in Fig. 6; No. 3 in Table 4) causes only a slight increase in permitted range of all parameters (Table 4; Fig. 7). In this regard, these data are less critical to constraining the values of the individual parameters.

Table 4. Summary of results for fitting subsets of viscosity data for HPG8 + 20 wt. % Na_2O to the TVF equation (see Table 3; after Hess *et al.*, 1995 and Dorfman *et al.*, 1996).

	Data subsets	N	χ^2	Parameter values			Projected 1σ limits [max – min]		
				A	**B**	**C**	**ΔA**	**ΔB**	**ΔC**
1	MP & CFS	11	4.0	-2.85	4784	429	4.54	4204	193
2	CC & CFS	16	3.4	-2.35	4060	484	3.70	3661	283
3	MP & CC	13	2.2	-2.38	4179	463	1.82	2195	123
4	All data	20	7.1	-2.76	4672	436	1.57	1809	98

Covariance in model parameters

The orientations of the 2-D projected ellipses shown in Fig. 6 are indicative of the covariance between model parameters over the entire solution space. The ellipse orientations for the four datasets vary, indicating that the covariances between model parameters can be affected by the quality or the distribution of the experimental data.

The 2-D projected confidence envelopes for the solution based on the entire experimental dataset (No. 4; Table 4) show strong correlations between model parameters (heavy line; Fig. 6). The strongest correlation is between **A** and **B** and the weakest is between **A** and **C**. Dropping the intermediate-temperature data (No. 3; Table 4) has virtually no ef-

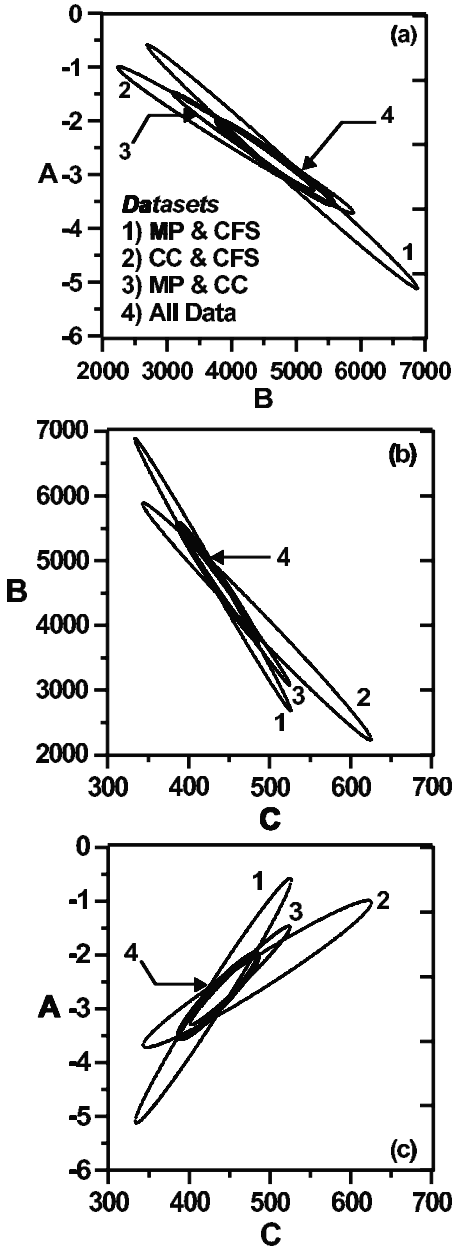

Fig. 6. Subsets of experimental data from Table 3 and Fig. 5 have been fitted to the TVF equation and the individual solutions are represented by 1σ confidence envelopes projected onto: a) the **A-B** plane, b) the **B-C** plane, and c) the **A-C** plane. The 2-D projections of the confidence ellipses vary in size and orientation depending of the distribution of experimental data in the individual subsets (see text).

fect on the covariances between model parameters; essentially the ellipses differ slightly in size but maintain a single orientation (Fig. 6a, b, c). The exclusion of the low-T (No. 2) or high-T (No. 1) data causes similar but opposite effects on the covariances between model parameters. Dropping the high-T data sets mainly increases the range of acceptable values of **A** and **B** (Table 4) but appears to slightly weaken the correlations between parameters (relative to case No. 4).

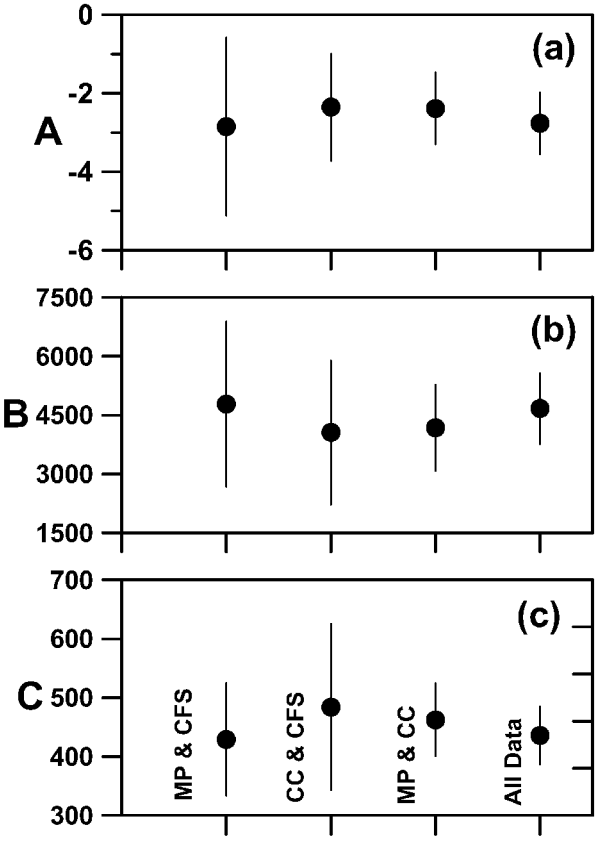

Fig. 7. Optimal values and 1σ ranges of parameters (a) **A**, (b) **B**, and (c) **C** derived for each subset of data (Table 3, Fig. 5 and 6). The range of acceptable values varies substantially depending on distribution of experimental data.

If the low-T data are excluded, the confidence limits on **B** and **C** increase and the covariance between **B** and **C**, and **A** and **C** are slightly stronger.

Model TVF functions

The implications of these results (Fig. 6 and 7) are summarized in Fig. 8. As discussed above, we calculated families of TVF functions that are consistent with the computed confidence limits on **A**, **B** and **C** (Fig. 6) for each dataset. The limits to the family of TVF curves are shown as two curves (solid lines) (Fig. 8) denoting the 1 σ confidence limits on the model function. The dashed line is the optimal TVF function obtained for each subset of data. The distribution of model curves reproduces the data well but the capacity to extrapolate beyond the limits of the dataset varies substantially.

The 1σ confidence limits calculated for the entire dataset (No. 4; Fig. 8d) are very narrow; over the entire temperature distribution of the measurements, the width of confidence limits is less than 1 log unit of viscosity. The complete dataset severely restricts the range of values for **A**, **B** and **C** and, therefore, produces a narrow band of model TVF functions which can be extrapolated beyond the limits of the dataset.

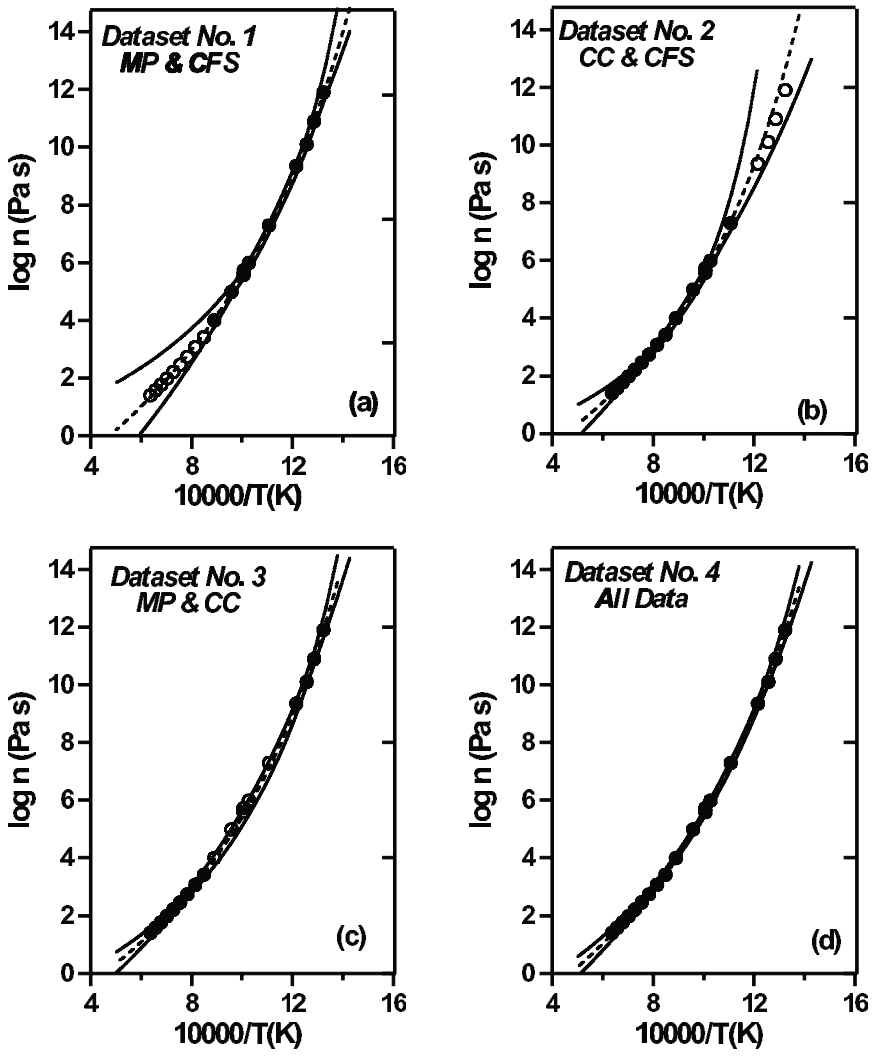

Fig. 8. The optimal TVF function (dashed lines) and the family of TVF functions (solid lines) computed from 1 σ confidence limits on **A**, **B** and **C** (Fig. 6 and Table 4) are compared to subsets of experimental data (solid symbols), including: a) MP and CFS, b) CC and CFS, c) MP and CC, and d) all data. Open circles denote data not used in fitting.

Excluding either the low-T or high-T subsets of data causes a marked increase in the width of confidence limits (Fig. 8a, b). The loss of the high-T data requires substantial expansion (1-2 log units) in the confidence limits on the TVF function at high temperatures (Fig. 8a). Conversely, for datasets lacking low-T measurements, the confidence limits to the low-T portion of the TVF curve increase to between 1 and 2 log units (Fig. 8b). In either case, the capacity for extrapolating the TVF function beyond the limits of the dataset is substantially reduced. Exclusion of the intermediate temperature data causes only a slight increase (10-20 %) in the confidence limits over the middle of the dataset.

Strong vs. fragile melts

Models for predicting silicate melt viscosities in natural systems must accommodate melts that exhibit varying degrees of non-Arrhenian temperature dependence. Therefore, our final analysis involves fitting of two datasets representative of a strong, near Arrhenian melt and a more fragile, non-Arrhenian melt: albite and diopside, respectively. The experimental data derive from the literature (Table 5) and were selected to provide a similar number of experiments, over a similar range of viscosities, and with approximately equivalent experimental uncertainties.

We have followed similar fitting procedures as described above and the results are summarized in Table 5 and Fig. 9. The optimal TVF parameters for diopside melt based on these 53 data points are: **A** = -4.66, **B** = 4,514, and **C** = 718 Table 5; Fig. 9a, b, solid line). The limiting values on these

Table 5. Results of fitting viscosity data[1] on albite and diopside melts to the TVF equation.

	Albite	Diopside
N	47	53
T (K) range	1099-2003	989-1873
A [min – max]	-6.46 [-14.6 to -2.8]	-4.66 [-6.3 to -3.6]
B [min – max]	14,816 [7240 to 40,712]	4514 [3306 to 6727]
C [min – max]	288 [-469 to 620]	718 [611 to 783]
χ^2	5.57	8.41

[1] Sources include: Urbain *et al.* (1982), Scarfe *et al.* (1983), N'Dala *et al.* (1984), Tauber & Arndt (1987), Dingwell (1989).

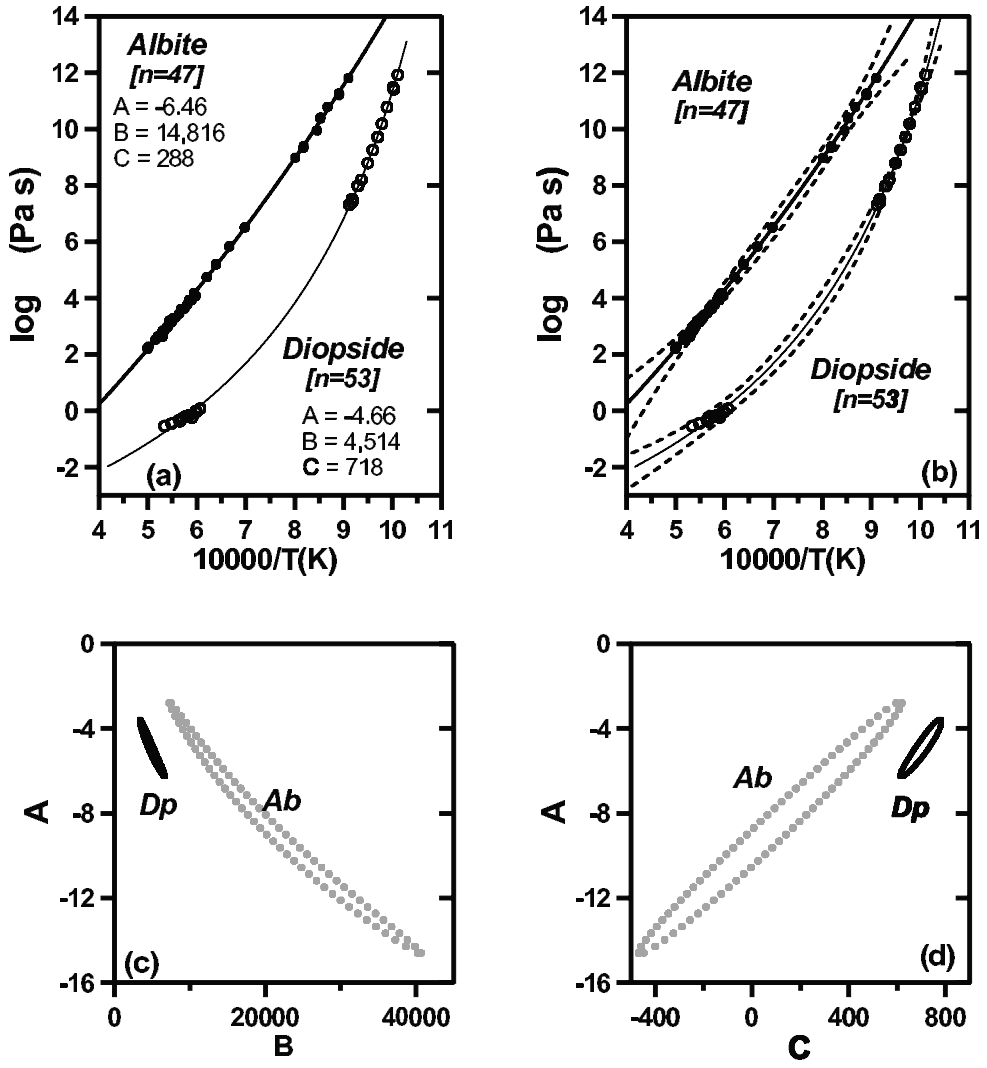

Fig. 9. Summary of TVF models used to describe experimental data on viscosities of albite (Ab) and diopside (Dp) melts (see Table 5). (a) Experimental data plotted as log [η(Pa s)] *vs.* 10,000/T (K) and compared to optimal TVF functions. (b) The family of acceptable TVF model curves (dashed lines) are compared to the experimental data. (c, d) Approximate 1 σ confidence limits projected onto the **A**-**B** and **A**-**C** planes. Fitting of the TVF function to the albite data results in a substantially wider range of parameter values than permitted by the diopside dataset. The albite melts show Arrhenian-like behaviour which, relative to the TVF function, implies an extra degree of freedom.

parameters, derived from the confidence ellipsoid (Fig. 9c, d), are quite restrictive (Table 5) and the resulting distribution of TVF functions can be extrapolated beyond the limits of the data (Fig. 9; dashed lines).

Fitting the TVF function to the albite melt data produces a substantially different outcome. The optimal parameters (**A** = -6.46, **B** = 14,816, and **C** = 288) describe the data well (Fig. 9a, b) but the 1 σ range of model values that are consistent with the dataset is huge (Table 5; Fig. 9c, d). Indeed, the range of acceptable parameter values for the albite melt is 5-10 times greater than the range of values estimated for diopside. Part of the solution space enclosed by the 1 σ confidence limits includes values that are unrealistic (*e.g.*, **C** < 0) and these can be ignored. Even excluding these solutions the range of values is substantial (-2.8 < **A** < -10.5; 7,240 < **B** < 27,500; and 0 < **C** < 620). However, the strong covariance between parameters results in a narrow distribution of acceptable TVF functions (Fig. 9b, dashed lines). Extrapolation of the TVF model past the data limits for the albite dataset has an inherently greater uncertainty than seen in the diopside dataset.

The differences found in fitting the TVF function to the viscosity data for diopside *versus* albite melts is a direct result of the properties of these two melts. Diopside melt shows pronounced non-Arrhenian properties and, therefore, requires all three adjustable parameters (**A**, **B**, and **C**) to describe its rheology. The albite melt is nearly Arrhenian in behaviour, defines a linear trend in log [η] – 10,000/T (K) space, and is adequately decribed by only two adjustable parameters. In applying the TVF function there is an extra degree of freedom which allows for a greater range of parameter values to be considered. For example, our present solution for the albite dataset (Table 5) includes both the optimal "Arrhenian" solutions (where **C** = 0; Fig. 9c, d), as well as solutions where the combinations of **A**, **B**, and **C** values generate a nearly Arrhenian trend. The near-Arrhenian behaviour of albite is only reproduced by the TVF model function over the range of experimental data (Fig. 9b). The non-Arrhenian character of the model and the attendant uncertainties increase when the function is extrapolated past the limits of the data.

These results have implications for modelling the compositional dependence of viscosity. Non-Arrhenian melts will tend to place tighter constraints on how composition is partitioned across the model parameters **A**, **B** and **C**. This is

because melts that show near Arrhenian properties can accommodate a wider range of parameter values. It is also possible that the high-temperature limiting behaviour of silicate melts can be treated as a constant, in which case, the parameter **A** need not have a compositional dependence. Comparing the model results for diopside and albite, it is clear that any value of **A** used to model the viscosity of diopside can also be applied to the albite melts if an appropriate value of **B** and **C** are chosen. The Arrhenian-like melt (albite) has little leverage on the exact value of **A**, whereas the non-Arrhenian melt requires a restricted range of values for **A**.

Conclusion

Developing a predictive model for the viscosity of natural silicate melts requires an understanding of how to partition the effects of composition across a non-Arrhenian model. At present, there is no definitive theory that establishes how parameters in non-Arrhenian equation (*e.g.*, **A**, **B**, **C**) should vary with composition. Furthermore, these parameters are not expected to be equally dependent on composition and definitely should not have the same functional dependence on composition. In the short-term, the decisions governing how to expand the non-Arrhenian parameters in terms of compositional effects will probably derive from empirical study.

During the search for empirical relationships between the model parameters and composition, it is important to realize that the optimal parameter values (*e.g.*, least squares solution) do not necessarily convey the entire story. The non-linear character of the non-Arrhenian models ensures strong numerical correlations between model parameters that mask the effects of composition. One result of the strong covariances between model parameters is that wide ranges of values (**A**, **B** or **C**) can be used to describe individual datasets. This is true even where the data are numerous, well-measured, and span a wide range of temperatures and viscosities. Stated another way, there is a substantial range of model values which, when combined in a non-arbitrary way, can accurately reproduce the experimental data.

This concept should be exploited to simplify development of a composition-dependent, non-Arrhenian model for multicomponent silicate melts. For example, it may be possible to impose a single value on the high-T limiting value of log [η] (*e.g.*, **A**) for some systems. The corollary to this would be the assignment of all compositional effects to the parameters **B** and **C**. Furthermore, it appears that non-Arrhenian datasets have the greatest leverage on compositional dependencies. Strong liquids that exhibit near-Arrhenian behaviour place only minor restrictions on the absolute ranges of values of **A**, **B** and **C**. Therefore, strategies for modelling the effects of composition should be built around high-quality datasets collected on non-Arrhenian melts.

Acknowledgements: This research was supported by the Natural Sciences and Engineering Research Council of Canada. JKR acknowledges support from the Bayerisches Geoinstitut, Bayreuth and Ludwig-Maximilians University, Munich and helpful discussions with Philippe Jarry. We are indebted to M.A. Bouhifd, Denis Andrault and, especially, Mike Toplis for thorough and constructive reviews. Their efforts substantially improved the clarity of our arguments.

Appendix: Computation of confidence limits

We have used minimization of the χ^2 function (Eq. 3) to obtain estimates of the TVF parameters $\mathbf{a}_j$ (j=1, *m*) based on a dataset of *n* measurements ($\mathbf{y}_i$; i=1,n). Essentially this is a weighted least-squares problem where the weighting scheme depends on estimates of uncertainties in the measurements (*e.g.*, σ_i; Tables 1 and 3). The χ^2 minimization strategy provides a means of establishing confidence limits on the values of the model parameters. This is done by mapping boundaries of constant χ^2 (values of $\Delta\chi^2$) around the optimal solution in the manner described fully by Press *et al.* (1986). These confidence limits provide objective estimates of the uncertainties on the model parameters based on the quality and distribution of the data (*e.g.*, Russell & Hauksdóttir, 2001; Russell *et al.*, 2001). Specifically, we use this strategy to portray the full range of TVF parameters that must be considered as consistent with the experimental data. The projected confidence limits on the model parameters (*e.g.*, Fig. 3, 6 and 9) represent linear approximations to the χ^2 solution surface; near the solution the linear model is indistinguishable from the actual χ^2 surface.

Operationally, we employ the following calculations (*e.g.*, Press *et al.,* 1986). Establish the optimal fit by solving for the minimum χ^2 (*e.g.*, $\chi^{2,\min}$). Compute the value $\Delta\chi^2$ ($\chi^{2,*}$ - $\chi^{2,\min}$) where the value of $\chi^{2,*}$ depends on the degrees of freedom (*n*-*m*) and the confidence level of interest (*e.g.*, 95 %). The matrix α(*m* x *m*) is then calculated for the $\chi^{2,\min}$ fit from:

$$\alpha_{k,l} = \sum_{i=1}^{n} \frac{1}{\sigma_i} \left[\frac{\partial \mathbf{y}_i^*}{\partial \mathbf{a}_k} \frac{\partial \mathbf{y}_i^*}{\partial \mathbf{a}_l} \right] \qquad \text{(A-1)}$$

where $\alpha_{k,l}$ are the individual entries on the matrix and $\mathbf{y}_i^*$ denotes the values of the functions predicted by the model. The covariance matrix (**C**) to the problem is then calculated from α^{-1}.

The constant χ^2 boundaries (confidence limits) are computed from the matrix equation:

$$\Delta\chi^2 = \mathbf{p} \cdot [\alpha] \cdot \mathbf{p'} \qquad \text{(A-2)}$$

where **p** is an *m*-component vector that describes the position of the confidence limits relative to the optimal solution. For a 3-parameter problem, Eq. A-2 describes a 3-D ellipsoid. We have portrayed the confidence limits as 2-D ellipses resulting from the projection of the entire 3-D ellipsoid onto a single plane (*e.g.*, Fig. 3, 6 and 9). These ellipses are calculated from:

$$\Delta\chi_2 = \mathbf{r} \cdot [\mathbf{C_p}]^{-1} \cdot \mathbf{r'} \qquad \text{(A-3)}$$

where $\mathbf{C_p}$ is the 2 x 2 submatrix of **C** containing rows and columns of the parameters of interest (*e.g.*, **A** and **B** or **B** and **C**). The unknowns to this matrix equation are the two components of the relative displacement vector **r** (*e.g.*, r_x and r_y). In its quadratic form, Eq. A-3 becomes:

$$\mathbf{r}_x^2 \cdot \mathbf{C_{p1,1}} + \mathbf{r}_x\mathbf{r}_y \cdot \mathbf{C_{p1,2}} + \mathbf{r}_y^2 \cdot \mathbf{C_{p2,2}} = \Delta\chi^2. \qquad \text{(A-4)}$$

The coordinates to the ellipse are computed by fixing one unknown (*e.g.*, $\mathbf{r}_y$) and solving for the roots to the resulting equation. Given arbitrary values of $\mathbf{r}_y$, the values of $\mathbf{r}_x$ are computed from:

$$\mathbf{r}_x = \frac{-\mathbf{r}_y \cdot \mathbf{C}_{p1,2} \pm \sqrt{(\mathbf{r}_y \cdot \mathbf{C}_{p1,2})^2 - \mathbf{C}_{p1,1} \cdot (\mathbf{r}_y^2 \cdot \mathbf{C}_{p2,2} - \Delta\chi^2)}}{\mathbf{C}_{p1,1}} \quad \text{(A-5)}$$

Operationally we search for coordinate pairs across the minimum and maximum range of values for $\mathbf{r}_y$ established by the relationship:

$$\mathbf{r}_y = \pm \sqrt{\frac{-\mathbf{C}_{p1,1} \cdot \Delta\chi^2}{\mathbf{C}_{p1,2}^2 - \mathbf{C}_{p1,1} \cdot \mathbf{C}_{p2,2}}} \quad \text{(A-6)}$$

These 2-D projections of the ellipsoids are linear approximations to the shadow cast by the entire 3-D confidence envelope onto this 2-dimensional plane. Axis-parallel tangents to these ellipses establish the maximum range of parameter values that are supported by the data at the specified confidence limits.

We have also computed and shown a second set of confidence limits (*e.g.*, smaller ellipses in Fig. 3). These represent the confidence limits for two parameters, where the 3rd parameter is fixed at the optimal solution. These ellipses are computed in exactly the same way as described above, except that the projection matrix $\mathbf{C}_p$ in Eq. A-3 is calculated from:

$$\mathbf{C}_p = [\alpha_p]^{-1} \quad \text{(A-7)}$$

where the matrix α_p is a 2 x 2 submatrix of comprising the rows and columns of the parameters that are not fixed (parameters that constitute the plane of projection). For example, in Fig. 3a, the small ellipse represents the intersection of the plane **C** = 359 with the 3-D ellipsoid. It shows the range of values of **A** and **B** permitted (and the apparent correlation) at this fixed value of **C.**

References

Adam, G. & Gibbs, J.H. (1965): On the temperature dependence of cooperative relaxation properties in glass-forming liquids. *J. Chem. Phys.*, **43**, 139-146.

Angell, C.A. (1988): Perspectives on the glass transition. *J. Phys. Chem. Solids*, **49**, 863-871.

Baker, D.R. (1996): Granitic melt viscosities: Empirical and configurational entropy models for their calculation. *Am. Mineral.*, **81**, 126-134.

Bottinga, Y. & Weill, D. (1972): The viscosity of magmatic silicate liquids: A model for calculation. *Am. J. Sci.*, **272**, 438-475.

Cranmer, D. & Uhlmann, D.R. (1981): Viscosities in the system albite-anorthite. *J. Geophys. Res.*, **86**, 7951-7956.

Dingwell, D.B. (1989) Effect of fluorine on viscosity of diopside liquid. *Am. Mineral.*, **74**, 333-338.

– (1993): Experimental strategies for the determination of granitic melt properties at low temperature. *Chemical Geol.*, **108**, 19-30.

– (1998): Recent experimental progress in the physical description of silicic magma relevant to explosive volcanism. *In* The Physics of Explosive Volcanic Eruptions (Eds. J.S. Gilbert & R.S.J. Sparks). *Geological Society, London, Spec. Publ.*, **145**, 9-26.

Dorfman, A., Hess, K.-U., Dingwell, D.B. (1996): Centrifuge-assisted falling-sphere viscometry. *Eur. J. Mineral.*, **8**, 507-514.

Fulcher, G.S. (1925): Analysis of recent measurements of the viscosity of glasses. *Am. Ceramic Soc. J.*, **8**, 339-355.

Giordano, D., Dingwell, D.B., Romano, C. (2000): The viscosity of a Teide phonolite in the welding interval. *J. Volc. Geothermal Res.*, **103**, 239-245.

Hess, K.U. & Dingwell, D.B. (1996): Viscosities of hydrous leucogranitic melts: A non-Arrhenian model. *Am. Mineral.*, **81**, 1297-1300.

Hess, K.U., Dingwell, D.B., Rossler, E. (1996): Parameterization of viscosity-temperature relations of aluminosilicate melts. *Chemical Geol.*, **128**, 155-163.

Hess, K.U., Dingwell, D.B., Webb, S.L. (1995): The influence of excess alkalies on the viscosity of a haplogranitic melt. *Am. Mineral.*, **80**, 297-304.

N'Dala, I., Cambier, F., Anseau, M.R., Urbain, G. (1984): Viscosity of liquid feldspars Part 1: Viscosity measurements. *British Ceramic Trans. J.*, **83**, 105-107.

Persikov, E.S. (1991): Viscosity of magmatic liquids: Experiment, generalized patterns. A model for the calculation and prediction. *Advances in Physical Geochemistry*, **9**, 1-40.

Press, W.H., Flannery, B.P., Teukolsky, S.A., Vetterling, W.T. (1986): Numerical Recipes: the Art of Scientific Computing. Cambridge University Press, Cambridge, 818 p.

Prusevich, A.A. (1988): Refinement of calculation of viscosity of magmatic melts according to their chemical composition. *Geologiya i Geofizika*, **29**, 67-69.

Richet, P. (1984): Viscosity and configurational entropy of silicate melts. *Geochim. Cosmochim. Acta*, **48**, 471-483.

Richet, P. & Bottinga, Y. (1995): Rheology and configurational entropy of silicate melts. *In* Structure, Dynamics & Properties of Silicate Melts, (Eds. J.F. Stebbins, P.F. McMillan, D.B. Dingwell). *Rev. Mineral.*, **32**, 67-94.

Rossler, E., Hess, K.-U., Novikov, V.N. (1998): Universal representation of viscosity in glass forming liquids. *J. Non-crystalline Solids*, **223**, 207-222.

Russell, J.K., Dipple, G.M., Kopylova, M.G. (2001): Heat production and heat flow in the mantle lithosphere to the Slave craton, Canada. *Phys. Earth Planet. Int.*, **123**, 27-44.

Russell, J.K. & Hauksdóttir, S. (2001): Estimates of crustal assimilation in Quaternary lavas from the northern cordillera, British Columbia. *Can. Mineral.*, **39**, 361-383.

Scarfe, C.M., Cronin, D.J., Wenzel, J.T., Kaufman, D.A. (1983): Viscosity-temperature relationships at 1 atmosphere in the system diopside-anorthite. *Am. Mineral.*, **68**, 1083-1088.

Shaw, H.R. (1972): Viscosities of magmatic silicate liquids: An empirical model of prediction. *Am. J. Sci.*, **272**, 438-475.

Tauber, P. & Arndt, J. (1987): The relationship between viscosity and temperature in the system anorthite-diopside. *Chemical Geol.*, **62**, 71-81.

Toplis, M.J. (1998): Energy barriers to viscous flow and the prediction of glass transition temperatures of molten silicates. *Am. Mineral.*, **83**, 480-490.

Toplis, M.J., Dingwell, D.B., Hess, K.-U., Lenci, T. (1997): Viscosity, fragility and configurational entropy of melts along the join SiO_2-$NaAlSiO_4$. *Am. Mineral.*, **82**, 979-990.

Urbain, G., Bottinga, Y., Richet, P. (1982): Viscosity of silica, silicates and aluminosilicates. *Geochim. Cosmochim. Acta*, **46**, 1061-1071.

Received 11 September 2000
Modified version received 20 August 2001
Accepted 24 September 2001